Nonsequential two-photon absorption in solid Ge irradiated by an intense x-ray free-electron-laser pulse

Stanislaw Wirok-Stoletow,[1,2] Rui Jin,[1] Daria Kolbasova [•],[1,2] Sang-Kil Son [•],[1,3,*] Andrew Aquila [•],[4] and Robin Santra [•][1,2,3,†]

[1]*Center for Free-Electron Laser Science, Deutsches Elektronen-Synchrotron DESY, 22607 Hamburg, Germany*
[2]*Department of Physics, Universität Hamburg, 22607 Hamburg, Germany*
[3]*The Hamburg Centre for Ultrafast Imaging, 22761 Hamburg, Germany*
[4]*LCLS, SLAC National Accelerator Laboratory, Menlo Park, California 94025, USA*

We theoretically investigate the formation of highly charged ions in a germanium (Ge) solid driven by intense, ultrashort x-ray pulses and its effect on the cross sections for nonsequential two-photon absorption from the K shell. Our investigation is related to an experiment conducted at the Linac Coherent Light Source, in which $K\alpha$ fluorescence was measured to identify nonsequential two-photon ionization. When a solid Ge target is irradiated by an intense x-ray free-electron-laser (XFEL) pulse, it undergoes severe ionization and turns into a plasma state. We employ a Monte Carlo molecular-dynamics approach to simulate the time evolution of Ge plasma formation, and the time-dependent configuration-interaction-singles method for cross-section calculations, taking into account various experimental x-ray beam parameters and Ge charge states created during the plasma formation dynamics. We find that under the given experimental condition at a photon energy of 7200 eV, charged ions are formed quickly (the average charge is $\approx +6$ at the peak of the pulse and $\approx +10$ at the end of the pulse). The cross sections of Ge for nonsequential two-photon absorption, however, turn out to be insensitive to different charge states, and the average value over all computed data is $(2.61 \pm 0.05) \times 10^{-59}$ cm^4 s. Our paper proposes a theoretical framework of photoabsorption cross-section calculations under the influence of plasma formation, when a solid target is employed in XFEL experiments.

I. INTRODUCTION

The study of light-matter interaction is strongly driven by the development of light sources. Laser technology has for many decades enabled us to produce and observe a large variety of nonlinear effects at visible, ultraviolet, and infrared wavelengths [1]. At shorter wavelengths, however, conventional lasers are not available, and x-ray free-electron lasers (XFELs) [2,3] provide high-intensity x-ray fields that are powerful enough to produce observable nonlinearity [2]. With very high x-ray intensity, the probability for the absorption of an x-ray photon by an atom during a single pulse can approach unity and saturate [4]. Accordingly, the relative contribution of multiphoton processes becomes significant in XFEL experiments. Such multiphoton processes are called sequential when single-photon absorption events take place shortly one after another, or nonsequential when multiple photons are absorbed simultaneously. While some sequential processes can display nonlinearities, nonsequential processes are most definitely nonlinear [4].

One of the difficulties of nonlinear studies in the x-ray regime is that nonlinear susceptibility and thereby multiphoton cross sections drop rapidly with increasing frequency of the electromagnetic field [5]. Therefore, only a few XFEL

experiments have so far been able to demonstrate nonsequential two-photon absorption processes in the x-ray regime: for gas-phase neon atoms [5], and for solid-state germanium [6], zirconium [7], and copper [8,9]. For the former atomic case, the formation of Ne^{9+} via sequential and nonsequential two-photon ionization was investigated. For the latter solid-state cases, the photon energy was tuned to half of the K-shell ionization threshold of the neutral ground state for the given atomic species, and the $K\alpha$ fluorescence corresponding to the neutral ground state was detected.

In the present paper, we deal with solid-state germanium (Ge) interacting with highly intense x-ray radiation. It is related to an unpublished experiment conducted at the Linac Coherent Light Source, at SLAC National Accelerator Laboratory [10]. Here, a solid Ge target was irradiated by $\approx$30–40-fs XFEL pulses with a pulse energy of $\approx$14 μJ on target, tightly focused to a beam diameter of $\approx$120-nm full width at half maximum (FWHM), corresponding to a peak intensity of $\approx 10^{18}$–10^{19} W/cm^2. The photon energy was centered at 7200 eV with a bandwidth of $\approx$30 eV. This photon energy was chosen distinctly beneath 11103 eV, which is the K-shell ionization edge of neutral Ge [11], such that the innermost electrons could not be ionized via a single-photon process. The goal of the experiment was to gather evidence for two-photon ionization by measuring $K\alpha$ fluorescence, generated by the refilling of the inner-shell holes by outer-shell electrons. This process is depicted schematically for neutral Ge in Fig. 1. However, it is anticipated that Ge

---

*sangkil.son@cfel.de
†robin.santra@cfel.de
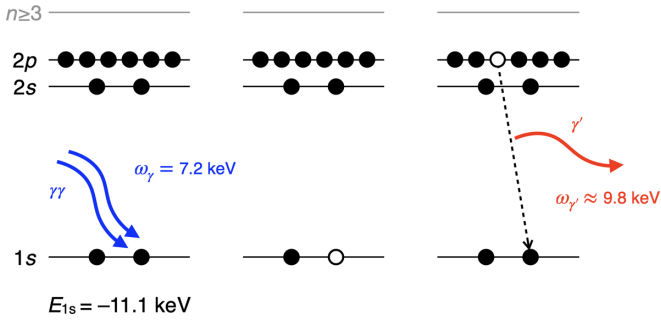
FIG. 1. Nonsequential two-photon ionization process from the neutral Ge 1*s* orbital followed by *Kα* fluorescence, driven by an intense XFEL pulse.

atoms exhibiting fluorescence were already ionized before *K*-shell two-photon absorption, because of outer-shell ionization during the interaction with intense XFEL pulses. The photon energy of the XFEL pulse is large enough to ionize electrons via a single-photon process from all shells but the *K* shell, and single-photon ionization from the outer shells is more probable than two-photon ionization from the *K* shell. Moreover, a solid-density environment causes plasma formation [12–14] and induces collisional ionization to create even higher charge states than would be formed in an isolated atom [15]. In fact, collisional ionization is the dominant ionization channel in XFEL-heated solid-density matter [12,16,17], and formation of high charge states due to collisional ionization is inevitable. Therefore, we do not know *a priori* which Ge ions the fluorescence is associated with, and it is important to examine the formation of charged ions of Ge and how they affect the creation of inner-shell holes via nonsequential two-photon absorption.

In this paper, we explore the creation and evolution of Ge charge states with the help of the Monte Carlo molecular-dynamics simulation tool XMDYN [18,19]. Here, one-photon cross sections and Auger-Meitner rates, as well as fluorescence rates, are provided by the XATOM toolkit [19]. Subsequently, we calculate cross sections for two-photon ionization from the *K* shell for various Ge ions. For that, we adopt the nonperturbative time-dependent configuration-interaction-singles (TDCIS) method [20–22]. TDCIS is a first-principles approach that is both computationally feasible and expected to be sufficient to describe the essential physics of an isolated single ionization process. It is beyond the single-active-electron approximation that has been widely used in strong-field physics [23,24], and electron-hole correlations are accounted for within TDCIS. We make use of the implementation of TDCIS within the XCID package [25], where the time propagation of an *N*-particle system under the influence of an external field is computed within the TDCIS configuration space on a flexible numerical grid. Because of our use of that numerical grid, in combination with a technique for eliminating artificial reflections of the outgoing photoelectron wave function from the end of the grid, we obtain an excellent description of the electronic continuum. XCID has been applied to examine a variety of theoretical problems in strong-field physics, as well as to provide theoretical cross-section values, which are comparable to experimental values [26–32].

The structure of this paper is as follows. In Sec. II A we briefly summarize the theoretical framework of TDCIS, while its numerical implementation and the convergence of numerical parameters are described in Sec. II B. The time evolution of Ge charge states during an intense XFEL pulse is presented in Sec. III A, the two-photon cross-section calculation for different Ge ions is presented in Sec. III B, and the underlying mechanism is discussed in Sec. III C. Conclusions are drawn in Sec. IV.

II. THEORY

A. Time-dependent configuration-interaction singles

In the TDCIS framework, the space of possible *N*-body states is limited appropriately via configuration-interaction singles (CIS), such that the time propagation of the electronic system can be calculated effectively. It builds fundamentally on the nonrelativistic Hartree-Fock (HF) method, where the *N*-particle wave function of the ground state $|\Phi_0\rangle$ is constructed as a single Slater determinant of *N* occupied one-particle orbitals existing in a mean field. Furthermore, this approach yields unoccupied virtual orbitals (for more details, see Ref. [33]). One-particle–one-hole (1*p*-1*h*) excitations $|\Phi_i^a\rangle$ are given by moving an electron from an occupied orbital *i* with an energy ε_i to a virtual orbital *a* with an energy ε_a. Linear combinations of the ground state $|\Phi_0\rangle$ and 1*p*-1*h* excitations $|\Phi_i^a\rangle$ with coefficients α_0 and α_i^a span the CIS space. When considering different atomic systems and charge states, all orbitals have to be optimized anew, which yields different CIS spaces for different systems. The TDCIS *N*-particle wave function, in turn, is constructed as having time-dependent coefficients $\alpha_0(t)$ and $\alpha_i^a(t)$ [20]:

$$|\Psi(t)\rangle = \alpha_0(t)|\Phi_0\rangle + \sum_{a,i} \alpha_i^a(t)|\Phi_i^a\rangle. \tag{1}$$

The time evolution of the TDCIS wave function under the influence of an external electromagnetic field is governed by the Hamiltonian [20]:

$$\hat{H}(t) = \hat{H}_{HF} + \hat{V}_C + \hat{H}_{LM}(t) - E_{HF}. \tag{2}$$

Here, $\hat{H}_{HF}$ describes the HF mean-field Hamiltonian and $\hat{V}_C$ the residual Coulomb interaction between the electrons, going beyond the mean-field picture. Furthermore, the Hamiltonian is shifted by the HF ground-state energy E_{HF} for convenience. $\hat{H}_{LM}$ accounts for the dipole term of the light-matter interaction in the minimal coupling and the Coulomb gauge, which in XCID is limited to pulses that are linearly polarized along the *z* axis. Accordingly, we obtain $\hat{H}_{LM} = \mathcal{E}(t)\hat{z}$, where $\mathcal{E}(t)$ is the time-dependent electric field strength and $\hat{z}$ is the *z* component of the dipole operator. Here we restrict ourselves to the length-form dipole operator. Note that TDCIS is not gauge invariant [34–37], but there are empirical reasons why the length gauge is preferable when using TDCIS for describing multiphoton processes [36,37].

Inserting the Hamiltonian from Eq. (2) into the time-dependent Schrödinger equation yields the (coupled) TDCIS

equations of motion, the solution of which describes the time evolution of the TDCIS wave function:

$$i\dot{\alpha}_0(t) = \mathcal{E}(t) \sum_{a,i} \langle \Phi_0 | \hat{z} | \Phi_i^a \rangle \alpha_i^a(t), \tag{3a}$$

$$i\dot{\alpha}_i^a(t) = (\varepsilon_a - \varepsilon_i)\, \alpha_i^a(t) + \mathcal{E}(t) \left[\langle \Phi_i^a | \hat{z} | \Phi_0 \rangle \alpha_0(t) \right.$$
$$\left. + \sum_{b,j} \langle \Phi_i^a | \hat{z} | \Phi_j^b \rangle \alpha_j^b(t) \right] + \sum_{b,j} \langle \Phi_i^a | \hat{V}_C | \Phi_j^b \rangle \alpha_j^b(t). \tag{3b}$$

B. Numerical implementation of TDCIS

The XCID package is capable of computing HF orbitals, constructing the CIS configurations, and solving the TDCIS equations of motion in Eq. (3) for closed-shell HF ground states (and hydrogenlike systems) on a numerical grid [21,25]. All wave functions are expanded in terms of a finite set of strongly localized radial basis functions, such that the numerical grid resembles a grid in physical space. We utilize the finite-element discrete variable representation [34]. To prevent artificial reflections of the N-electron wave function at the edge of the grid and minimize computational costs, absorbing boundaries are introduced towards the end of the radial grid. We make use of the smooth-exterior-complex-scaling (SES) method [34]. Time propagation is performed using the Runge-Kutta fourth-order method [38].

The TDCIS framework allows for arbitrary pulse shapes. Note that XFEL pulses based on the self-amplified spontaneous emission (SASE) principle [2] are fully chaotic in terms of their temporal and spectral shapes. Ideally, one could perform TDCIS calculations many times with different stochastically generated SASE pulse shapes and then average the results over the stochastic ensemble. This approach, however, is computationally expensive. Instead, here we employ a deterministic coherent pulse shape with a Gaussian envelope, which corresponds to a single SASE spike [39], assuming that nonsequential two-photon response is governed by a single spike. Then, the time-dependent electric field strength is given by

$$\mathcal{E}(t) = \mathcal{E}_0 \exp\left[-2\ln 2 \left(\frac{t}{\tau_I} \right)^2 \right] \cos(\omega_\gamma t), \tag{4}$$

where $\mathcal{E}_0$ is the maximum field strength, ω_γ is the photon energy, and τ_I is the pulse duration (FWHM) of the pulse intensity. In order to capture the bandwidth of SASE pulses, we chose τ_I as the characteristic duration of the SASE spikes. The XFEL bandwidth is then given by $\Delta\omega_\gamma = (4\ln 2)/\tau_I$. These x-ray beam parameters are varied in Sec. III B.

In our implementation, there are several computational parameters, including the number of grid points N_g, the maximal radius of the grid R_{max}, the grid uniformity parameter ζ, the onset radius of absorber r_{abs}, the SES complex-scaling angle ϑ and smoothing factor λ, the maximum angular momentum l_{max}, the cutoff energy to be included in the computational space e_{cut}, and the propagation time step Δt. The computational parameters are tested for numerical convergence with

respect to calculated cross-section values. As a result, we choose a grid size of $N_g = 400$ points and a maximum radius of $R_{max} = 120$ a.u. extending far beyond the electronic system in its ground state. At a time step of $\Delta t = 0.0007$ a.u. ($= 1.69 \times 10^{-2}$ as) the passing of one wavelength of the electric field is sampled at 34 points. Since we are interested in two-photon ionization from the K shell ($l = 0$), $l_{max} = 3$ is sufficient. The virtual orbital energies beyond $e_{cut} = 400$ a.u. ($= 10\,884.4$ eV) are cut off. Finally, the complex scaling (SES) starts off at $r_{abs} = 110$ a.u. with an angle of $\vartheta = 40°$ and a smoothing factor of $\lambda = 1$.

III. RESULTS AND DISCUSSION

A. Time evolution of Ge charge-state population during an intense XFEL pulse

When a solid target is irradiated by an intense, ultrashort XFEL pulse, the system is highly ionized by photoionization, Auger-Meitner decay, and subsequent electron impact ionization, creating large Coulomb potentials. Thus, ionized electrons are trapped and form a dense (solid-density) plasma [12–14]. To illustrate the creation and evolution of such a plasma in solid Ge we use the Monte Carlo molecular-dynamics simulation tool, XMDYN [18,19], which has been extended through the implementation of periodic boundary conditions to study warm dense matter [15,40,41]. XMDYN handles atomic processes (photoionization, Auger-Meitner decay, and fluorescence) quantum mechanically, and environmental phenomena (collisional ionization, recombination, and Coulomb interaction between charged particles) using a classical treatment [19]. Charge transfer and field-induced processes are not included in the present paper.

We simulate a Ge supercell consisting of $4 \times 4 \times 4$ unit cells, containing eight atoms each, i.e., 512 atoms in total. The supercell size is 23.05 Å [42], so the ion density used is 5.078 g/cm^3. This supercell is irradiated by an intense x-ray pulse with a photon energy of 7200 eV, a pulse duration of 35 fs FWHM, and a fixed fluence of 7.47×10^{11} ph/μm^2, which corresponds to a peak intensity of 2.3×10^{18} W/cm^2 to mimic the experimental condition. Note that the supercell size is much smaller than the estimated focal diameter of 120 nm, so we may assume that the fluence is applied uniformly throughout the supercell. To evaluate classical Coulomb interactions, we employ a soft-core potential radius [19] of $r_0 = 0.25$ Å and a simulation time step of $dt = 0.5$ as (for atomic ions and electrons), as they guarantee sufficiently small errors on energy conservation ($<0.1\%$). For better statistical results, we run ten parallel realizations. The plasma environmental effect, namely ionization potential depression (IPD) [12,13,41,43], is not considered for simplicity. Note that for the given x-ray parameters the IPD values are estimated to lie in the range from 100 to 260 eV for charge states between $+6$ and $+14$ by employing a hybrid quantum-classical model [41]. These values are much smaller in comparison with the given photon energy of 7200 eV, so we expect that IPD has little influence on photoionization processes.

Time evolutions of average charge and individual charge-state populations, as well as the temporal pulse shape, are shown in Fig. 2. We observe that the Ge solid starts to ionize
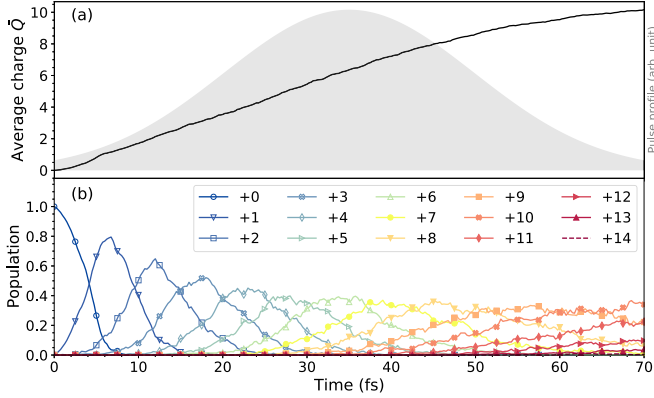
FIG. 2. (a) Solid line: The average charge of a Ge atom in a $4 \times 4 \times 4$ supercell as a function of time during irradiation by an intense XFEL pulse at a photon energy of 7200 eV. Gray shade: The temporal profile of a Gaussian pulse with a pulse duration of 35-fs FWHM and its peak centered at 35 fs, as used in the simulation. (b) Time evolution of Ge charge-state populations at a fixed fluence of 7.47×10^{11} ph/μm^2.

TABLE I. Ionization potential for each subshell and $K\alpha$ fluorescence energy for different closed-shell Ge charge states calculated with XCID. Units are in eV.

	Ge^{2+}	Ge^{4+}	Ge^{14+}	Ge^{20+}	Ge^{22+}
IP(1s)	11047.1	11076.5	11493.4	11866.2	11996.2
IP(2s)	1439.2	1467.8	1889.3	2218.8	2331.4
IP(2p)	1278.1	1306.9	1728.7	2062.6	2180.4
IP(3s)	215.5	243.8	587.5	823.1	
IP(3p)	160.3	189.1	527.9		
IP(3d)	64.5	92.8			
IP(4s)	31.8				
$K\alpha$	9769.0	9769.6	9764.7	9803.6	9815.8

quickly after the onset of irradiation: the neutral Ge population drops almost to zero soon after the onset of the pulse. At the peak of the pulse, the charge-state distribution is dominated by Ge^{5+} to Ge^{8+} with the average charge of $\approx +6$. At the end of the pulse the charge states of Ge^{9+}, Ge^{10+}, and Ge^{11+} make up the majority of the population of the supercell with the average charge of $\approx +10$. Consequently, we cannot simply employ neutral Ge for our cross-section calculations beforehand. Instead, we will calculate and evaluate cross sections for a variety of different Ge charge states in the next section.

B. Two-photon cross-section calculation for various Ge charge states

The two-photon cross section can be calculated with two different approaches: by nonperturbatively solving the time-dependent Schrödinger equation [44], or by employing the lowest nonvanishing order of perturbation theory (LOPT) [45]. To take into account the finite bandwidth and the short coherent time of SASE pulses, LOPT results calculated for monochromatic radiation must be convolved with the spectral distribution function, resulting in an effective two-photon cross section. Here, we use the nonperturbative TDCIS approach for a single coherent pulse representing a SASE spiky pulse.

In our numerical investigation of the nonlinear response of different Ge charge states to coherent pulses we consider closed-shell systems only: Ge^{2+}, Ge^{4+}, Ge^{14+}, Ge^{20+}, and Ge^{22+}. The ionization potentials of the individual subshells of different closed-shell Ge charge states, as calculated with the help of XCID, are listed in Table I. Since the photon energy is 7200 eV and its bandwidth is 30 eV in experiment, ionization from the K shell requires a two-photon process, regardless of the particular Ge charge state. On the other hand, single-photon ionization is possible for all other subshells. This explains why Ge charge states are quickly formed with the experimental beam parameters (see Sec. III A). Furthermore, as shown in Table I, $K\alpha$ fluorescence energies for different

Ge charge states are relatively similar to each other ($<0.5\%$). Hence, it may not be feasible to distinguish specific charge states associated with specific fluorescence energies, unless resolution of the photon detection is sufficiently high. We also assume no drastic changes of two-photon ionization rates for open-shell systems in comparison with closed-shell systems, because the $1s$ subshell is little affected by variation from incomplete occupations in outer shells and the photon energy used here is far from resonance for the two-photon process. Therefore, the investigation for the five different closed-shell Ge ions should suffice to describe two-photon ionization for a series of Ge charge states that may be produced in plasma-formation dynamics.

The information about excitation and ionization of the irradiated system is implicitly given in TDCIS calculations. The 1p-1h excitations $|\Phi_i^a\rangle$ with respective coefficients $\alpha_i^a(t)$ do not represent excited states of the actual N-electron system [20]. Instead, the full N-electron system is partitioned into two subsystems: the excited electron and the parent ion containing the remaining electrons. Subsequently, we obtain the probability to find a hole in a specific orbital of the parent ion, by examining the ionic density matrix:

$$\hat{\rho}(t) = \mathrm{Tr}_a[|\Psi(t)\rangle\langle\Psi(t)|], \tag{5a}$$

$$\rho_{ij}(t) = \sum_a \langle\Phi_i^a|\Psi(t)\rangle\langle\Psi(t)|\Phi_j^a\rangle. \tag{5b}$$

The elements $\rho_{ii}(t)$ describe the probability to find a hole in the ith orbital $|\phi_i\rangle$ of the parent ion subsystem, and thus the probability of the system emitting an electron from the respective orbital [20].

The significance of the different modes of interaction between the electromagnetic field and the electronic system can be seen in Fig. 3. Here, the dependences of the ground-state depopulation $(1-\rho_0)$ and the K-shell hole population ρ_{11} on the maximum field intensity I_0 $(=\mathcal{E}_0^2$ in atomic units) are depicted for the charge states Ge^{2+} and Ge^{22+}. The quantity $(1-\rho_0)$ indicates the probability that the system leaves its ground state and is excited via interaction with the electromagnetic field, regardless of the particular processes and electrons involved. On the other hand, ρ_{11} indicates the probability that an electron is excited from the K shell, leaving behind a K hole. This excitation is physically only possible via two-photon absorption. In Fig. 3 we can see that the ground-state depopulation $(1 - \rho_0)$ clearly shows a linear dependence
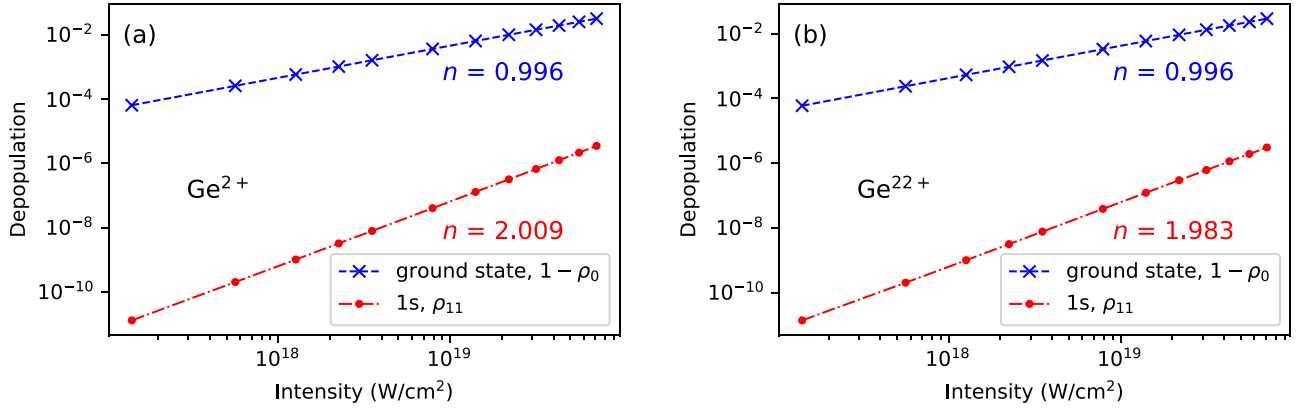
FIG. 3. Depopulation of the TDCIS ground state and $1s$-hole population of (a) Ge^{2+} and (b) Ge^{22+} as a function of the peak intensity of the electromagnetic field. A Gaussian pulse with a photon energy of 7200 eV and a bandwidth of 41.9 eV is employed.

on I_0 at experimental conditions ($I_0 < 10^{20}$ W/cm^2). In Fig. 3, the data points of $(1 - \rho_0)$ are fitted to $y = Ax^n$, where $n = 0.996$ for both (a) Ge^{2+} and (b) Ge^{22+}. The probability for the system to interact with the electromagnetic field at all is proportional to the intensity, which is indicative of single-photon processes. On the other hand, the K-shell hole population, ρ_{11}, shows a quadratic dependence [$n = 2.009$ for (a) and $n = 1.983$ for (b)], which corresponds to a two-photon process. The values of $(1 - \rho_0)$ are orders of magnitude higher than those of ρ_{11}. Thus, one-photon ionization from outer shells is the dominant mode of interaction between the electromagnetic field and the electronic system at experimental intensities. At the same time, we verify that XCID can reliably reproduce the two-photon process from the K shell.

Finally, we calculate nonsequential two-photon cross sections from the quadratic response of ρ_{11} to the external field. For a coherent laser pulse, which is a good approximation for a single XFEL SASE spike [39], the two-photon cross section is given by [32]

$$\sigma^{(2)}_{coh}(\omega_\gamma, \tau_I) = \frac{\lim_{t \to \infty} \rho_{11}(t, \omega_\gamma, \tau_I)}{\int_{-\infty}^{\infty} J(t, \omega_\gamma, \tau_I)^2 \, dt}, \qquad (6)$$

where $J(t)$ is the photon flux given by $J(t) = \mathcal{E}(t)^2/\omega_\gamma$. Here, τ_I is the pulse duration of a single XFEL spike, and the energy bandwidth is given by the pulse duration of a single XFEL spike, $\Delta\omega_\gamma$ (in eV) $= 1.825/\tau_I$ (in fs). Note that ρ_{11} in Eq. (6) contains a minor correction as suggested in Refs. [21,32,46], because of the norm loss in the ionic density matrix induced by the absorbing boundary. With that, we perform the two-photon-absorption cross-section calculations for each Ge charge state for five different photon energies ω_γ (6900, 7050, 7200, 7350, and 7500 eV), five different pulse lengths τ_I (62.9, 53.2, 43.5, 33.9, and 24.2 as), and hence five different energy bandwidths $\Delta\omega_\gamma$ (29.0, 34.3, 41.9, 53.9, and 75.4 eV) in order to cover uncertainty in experimental parameters and to compensate the IPD effects that are not included in the present paper.

The dependences of the calculated cross section on the photon energy at fixed bandwidth ($\Delta\omega_\gamma = 41.9$ eV) and on the bandwidth at fixed photon energy ($\omega_\gamma = 7200$ eV) are depicted in Fig. 4. We see that the cross-section values show only little variation as a function of the x-ray beam

parameters ($<9.3\%$ for $\omega_\gamma = 7200 \pm 300$ eV and $<16.5\%$ for $\Delta\omega_\gamma = 29.0$–75.4 eV), which is also true for all other combinations of energy and bandwidth (not shown here). In addition, our results showcase a close similarity between the cross sections for the different Ge ions in the given range of photon energies and bandwidths considered. Table II lists calculated cross sections at a photon energy of 7200 eV and a bandwidth of 41.9 eV for different charge states. From our calculations, we obtain for the two-photon absorption cross section an average value of $\sigma^{(2)} = (2.61 \pm 0.05) \times 10^{-59}$ cm^4 s. This value is comparable to the estimate from the simple Z scaling law [47,48] for a nonrelativistic hydrogenlike ion: $\sigma^{(2)}(Z, \omega_\gamma) = \sigma^{(2)}(1, \omega_\gamma/Z^2)/Z^6$, where $\sigma^{(2)}(Z = 1, \omega_\gamma = 7$ eV$) = 1.24 \times 10^{-50}$ cm^4 s [49]. For Ge with two $1s$ electrons, this estimate gives $2 \times \sigma^{(2)}(Z = 32, \omega_\gamma = 7200$ eV$) = 2.31 \times 10^{-59}$ cm^4 s. A relativistic calculation for neutral Ge gives 2.2×10^{-59} cm^4 s [50]. Based on the relativistic factor $\xi(Z)$ [51] we expect our TDCIS result to overestimate the true K-shell two-photon absorption cross section by about 10%.

C. Underlying mechanism

The insensitivity of our calculated two-photon cross section to the beam parameters and the charge states can be explained by the nonresonant situation investigated in the present paper. Even though the $1s$ ionization potential shifts by almost 1000 eV from 11047.1 eV in Ge^{2+} to 11996.2 eV in Ge^{22+}, as shown in Table I, the given range of photon energies is still far from any resonances.

TABLE II. Theoretical cross sections for two-photon ionization from the $1s$ subshell in different Ge charge states calculated at $\omega_\gamma = 7200$ eV and $\Delta\omega_\gamma = 41.9$ eV.

Charge state	Two-photon cross section $\sigma^{(2)}$ (cm^4 s)
Ge^{2+}	2.54×10^{-59}
Ge^{4+}	2.62×10^{-59}
Ge^{14+}	2.63×10^{-59}
Ge^{20+}	2.66×10^{-59}
Ge^{22+}	2.61×10^{-59}
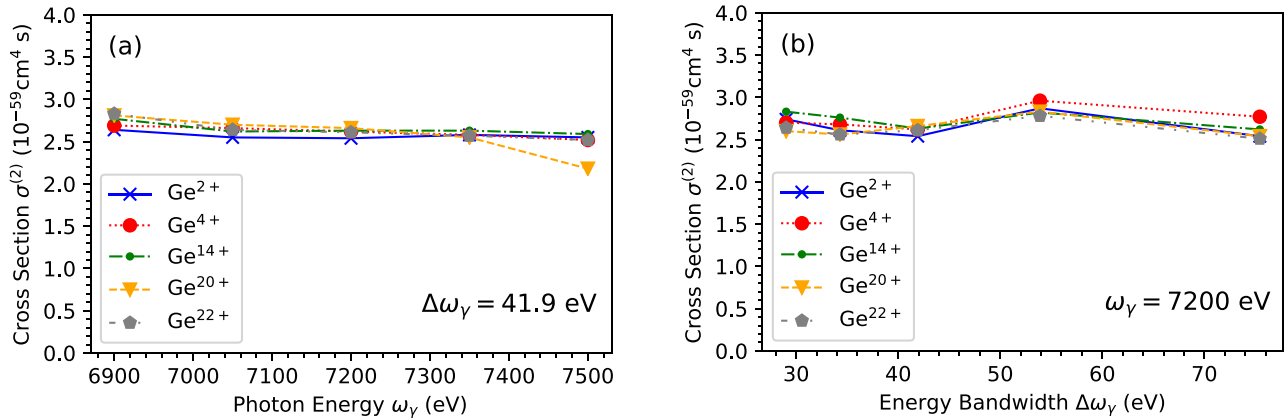
FIG. 4. Cross sections $\sigma^{(2)}$ for nonsequential two-photon ionization from the K shell in different Ge charge states as a function of (a) photon energy ω_γ at a fixed bandwidth of 41.9 eV and (b) bandwidth $\Delta\omega_\gamma$ at a fixed photon energy of 7200 eV.

According to the LOPT expression for the two-photon cross section [see, e.g., Eq. (9) in Ref. [32]], two different pathways are involved in the nonsequential two-photon ionization process. One is $1s$ to np excitation followed by np ionization, as illustrated in Fig. 5(a). The intermediate state is a $1s$ hole, and n depends on its occupancy for given charge states ($n \geqslant 4$ for Ge^{2+}, Ge^{4+}, and Ge^{14+}; $n \geqslant 3$ for Ge^{20+} and Ge^{22+}). The other is np ionization followed by $1s$ to np excitation, via an np-hole intermediate state, as depicted in Fig. 5(b). In this case, $n = 2$ is available even though $2p$ is initially fully occupied for the charge states under consideration, because a $2p$ vacancy becomes available after $2p$ ionization. Moreover, $n = 2$ will be the most probable, because the transition from $2p$ to the continuum has the largest amplitude. This mechanism is similar to the hidden $1s$–$2p$ resonance that is initially blocked for neutral Ne but is made accessible by $2p$ photoionization [52], although there is no actual resonance in the present case.

Between the two pathways, the latter involving the $2p$-hole intermediate state will be dominant, because the $1s$–$2p$ tran- sition has the largest transition amplitude. We also find that the $1s$ and $2p$ orbitals are relatively insensitive to the number of electrons in higher-lying orbitals. For instance, $\langle r \rangle_{1s}$ and $\langle r \rangle_{2p}$ hardly change for the various ions under considera- tion, as shown in Table III. Therefore, we conclude that the mechanism in the two-photon process provides an additional explanation for the observed insensitivity of the calculated two-photon cross section to the atomic charge state.

IV. CONCLUSION

When a nonsequential multiphoton process is invoked in a solid target by x-ray radiation, this has been often considered as a phenomenon reflecting properties of neutral ground-state species. Such a process, however, requires very high inten- sities to become measurable, so that production of highly charged ions and, thus, plasma formation are unavoidable in the target material.

In this paper, we have presented a theoretical frame- work to calculate nonsequential two-photon absorption cross
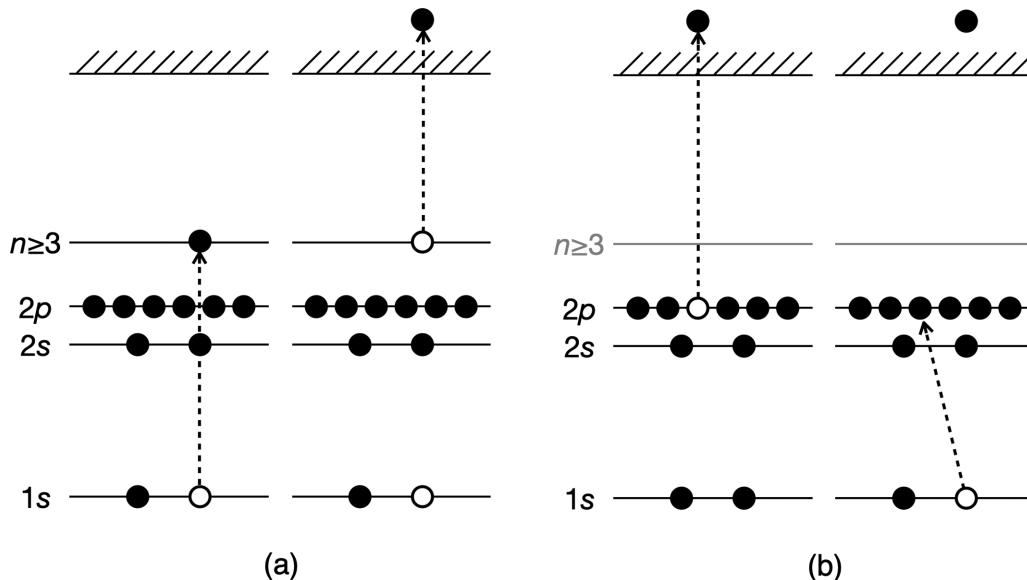
FIG. 5. Two different pathways involved in the nonsequential two-photon ionization process: (a) $1s$–np transition followed by np ionization via a $1s$-hole intermediate state, and (b) $2p$ ionization followed by $1s$–$2p$ transition via a $2p$-hole intermediate state.

TABLE III. Expectation values of the $1s$ and $2p$ radii for different closed-shell Ge charge states calculated with XCID. Units are in a.u.

	Ge^{2+}	Ge^{4+}	Ge^{14+}	Ge^{20+}	Ge^{22+}
$\langle r \rangle_{1s}$	0.0478	0.0478	0.0479	0.0478	0.0478
$\langle r \rangle_{2p}$	0.185	0.185	0.184	0.182	0.181

sections of solid Ge in the x-ray regime, particularly when the solid target turns into a dense plasma at high x-ray intensity. The plasma formation is simulated with a Monte Carlo molecular-dynamics approach, and the nonsequential two-photon cross section is evaluated by using the time-dependent configuration-interaction-singles method. Given x-ray beam parameters of 7200 eV and 10^{18} to 10^{19} W/cm^2, highly charged atomic ions are rapidly created in the Ge solid target, such that the average charge is about $+6$ at the peak of the pulse and about $+10$ at the end of the pulse. We find that our calculated two-photon cross sections are insensitive to specific charge states, resulting in an average value of $(2.61 \pm 0.05) \times 10^{-59}$ cm^4 s. In this case, where the photon energy is far from any intermediate- or final-state resonances, this value is representative of the ground-state cross section and the usage of the cross section calculated for an isolated neutral atom appears to be justified. Our results suggest that, unless resonant conditions are selected, one should not expect any sensitivity of K-shell two-photon absorption to solid-state properties.

We note that if the photon energy is tuned to resonances, for example, two photons cause a bound-to-bound transition or there is an intermediate state in one-photon resonance, it will be critical to take into account the plasma formation effects including different ionization potentials of highly charged ions and their ionization potential depression due to a dense plasma environment. We also acknowledge that our investigation is based on closed-shell targets and the TD-CIS method, in which certain many-body effects are missing. Therefore, it cannot be entirely ruled out that open-shell ions and missing many-body effects could lead to a higher sensitivity of the x-ray two-photon absorption cross section than found in the present calculations. On the other hand, the observed insensitivity is plausible in view of the mechanism described in Sec. III C. If there happens to be a more substantial sensitivity to charge state than suggested here, then it would imply that experimental x-ray two-photon K-shell ionization cross sections are intensity dependent, because the x-ray intensity determines the charge-state distribution in which x-ray two-photon absorption takes place. A solution would be energy-resolved K-shell fluorescence detection.

[1] R. Boyd, *Nonlinear Optics*, 3rd ed. (Academic Press, Cambridge, 2008).

[2] C. Pellegrini, A. Marinelli, and S. Reiche, The physics of x-ray free-electron lasers, Rev. Mod. Phys. **88**, 015006 (2016).

[3] E. A. Seddon, J. A. Clarke, D. J. Dunning, C. Masciovecchio, C. J. Milne, F. Parmigiani, D. Rugg, J. C. H. Spence, N. R. Thompson, K. Ueda, S. M. Vinko, J. S. Wark, and W. Wurth, Short-wavelength free-electron laser sources and science: A review, Rep. Prog. Phys. **80**, 115901 (2017).

[4] R. Santra and L. Young, Interaction of intense x-ray beams with atoms, in *Synchrotron Light Sources and Free-Electron Lasers: Accelerator Physics, Instrumentation and Science Applications*, edited by E. Jaeschke, S. Khan, J. Schneider, and J. Hastings (Springer, Cham, 2014), pp. 1233–1260.

[5] G. Doumy, C. Roedig, S.-K. Son, C. I. Blaga, A. D. DiChiara, R. Santra, N. Berrah, C. Bostedt, J. D. Bozek, P. H. Bucksbaum, J. P. Cryan, L. Fang, S. Ghimire, J. M. Glownia, M. Hoener, E. P. Kanter, B. Krässig, M. Kuebel, M. Messerschmidt, G. G. Paulus *et al.*, Nonlinear Atomic Response to Intense Ultrashort X Rays, Phys. Rev. Lett. **106**, 083002 (2011).

[6] K. Tamasaku, E. Shigemasa, Y. Inubushi, T. Katayama, K. Sawada, H. Yumoto, H. Ohashi, H. Mimura, M. Yabashi, K. Yamauchi, and T. Ishikawa, X-ray two-photon absorption competing against single and sequential multiphoton processes, Nat. Photonics **8**, 313 (2014).

[7] S. Ghimire, M. Fuchs, J. Hastings, S. C. Herrmann, Y. Inubushi, J. Pines, S. Shwartz, M. Yabashi, and D. A. Reis, Nonsequential two-photon absorption from the K shell in solid zirconium, Phys. Rev. A **94**, 043418 (2016).

[8] J. Szlachetko, J. Hoszowska, J.-C. Dousse, M. Nachtegaal, W. Błachucki, Y. Kayser, J. Sà, M. Messerschmidt, S. Boutet, G. J. Williams, C. David, G. Smolentsev, J. A. van Bokhoven, B. D. Patterson, T. J. Penfold, G. Knopp, M. Pajek, R. Abela, and C. J. Milne, Establishing nonlinearity thresholds with ultraintense x-ray pulses, Sci. Rep. **6**, 33292 (2016).

[9] K. Tamasaku, E. Shigemasa, Y. Inubushi, I. Inoue, T. Osaka, T. Katayama, M. Yabashi, A. Koide, T. Yokoyama, and T. Ishikawa, Nonlinear Spectroscopy with X-Ray Two-Photon Absorption in Metallic Copper, Phys. Rev. Lett. **121**, 083901 (2018).

[10] A. Aquila, M. Liang, and S. Boutet (unpublished).

[11] A. C. Thompson, D. T. Attwood, E. M. Gullikson, M. R. Howells, K.-J. Kim, J. Kirz, J. B. Kortright, I. Lindau, Y. Liu, P. Pianetta *et al.*, *X-ray Data Booklet* (Lawrence Berkeley National Laboratory, University of California Berkeley, CA, 2009).

[12] S. M. Vinko, O. Ciricosta, B. I. Cho, K. Engelhorn, H.-K. Chung, C. R. D. Brown, T. Burian, J. Chalupský, R. W. Falcone, C. Graves, V. Hájková, A. Higginbotham, L. Juha, J. Krzywinski, H. J. Lee, M. Messerschmidt, C. D. Murphy, Y. Ping, A. Scherz, W. Schlotter *et al.*, Creation and diagnosis of a solid-density plasma with an x-ray free-electron laser, Nature (London) **482**, 59 (2012).

[13] O. Ciricosta, S. M. Vinko, H.-K. Chung, B.-I. Cho, C. R. D. Brown, T. Burian, J. Chalupský, K. Engelhorn, R. W.

Falcone, C. Graves, V. Hájková, A. Higginbotham, L. Juha, J. Krzywinski, H. J. Lee, M. Messerschmidt, C. D. Murphy, Y. Ping, D. S. Rackstraw, A. Scherz *et al.*, Direct Measurements of the Ionization Potential Depression in a Dense Plasma, Phys. Rev. Lett. **109**, 065002 (2012).

[14] B. I. Cho, K. Engelhorn, S. M. Vinko, H.-K. Chung, O. Ciricosta, D. S. Rackstraw, R. W. Falcone, C. R. D. Brown, T. Burian, J. Chalupský, C. Graves, V. Hájková, A. Higginbotham, L. Juha, J. Krzywinski, H. J. Lee, M. Messersmidt, C. Murphy, Y. Ping, N. Rohringer *et al.*, Resonant $K\alpha$ Spectroscopy of Solid-Density Aluminum Plasmas, Phys. Rev. Lett. **109**, 245003 (2012).

[15] M. M. Abdullah, Z. Jurek, S.-K. Son, and R. Santra, Calculation of x-ray scattering patterns from nanocrystals at high x-ray intensity, Struct. Dyn. **3**, 054101 (2016).

[16] S. M. Vinko, O. Ciricosta, T. R. Preston, D. S. Rackstraw, C. R. D. Brown, T. Burian, J. Chalupský, B. I. Cho, H.-K. Chung, K. Engelhorn, R. W. Falcone, R. Fiokovinini, V. Hájková, P. A. Heimann, L. Juha, H. J. Lee, R. W. Lee, M. Messerschmidt, B. Nagler, W. Schlotter *et al.*, Investigation of femtosecond collisional ionization rates in a solid-density aluminium plasma, Nat. Commun. **6**, 6397 (2015).

[17] R. Jin, Z. Jurek, R. Santra, and S.-K. Son, Plasma environmental effects in the atomic structure for simulating x-ray free-electron-laser-heated solid-density matter, Phys. Rev. E **106**, 015206 (2022).

[18] B. F. Murphy, T. Osipov, Z. Jurek, L. Fang, S.-K. Son, M. Mucke, J. Eland, V. Zhaunerchyk, R. Feifel, L. Avaldi, P. Bolognesi, C. Bostedt, J. D. Bozek, J. Grilj, M. Guehr, L. J. Frasinski, J. Glownia, D. T. Ha, K. Hoffmann, E. Kukk *et al.*, Femtosecond x-ray-induced explosion of C_{60} at extreme intensity, Nat. Commun. **5**, 4281 (2014).

[19] Z. Jurek, S.-K. Son, B. Ziaja, and R. Santra, *XMDYN* and *XATOM*: Versatile simulation tools for quantitative modeling of X-ray free-electron laser induced dynamics of matter, J. Appl. Cryst. **49**, 1048 (2016).

[20] S. Pabst and R. Santra, Time-dependent configuration interaction singles, in *Computational Strong-Field Quantum Dynamics: Intense Light-Matter Interactions*, edited by D. Bauer (De Gruyter, Berlin, Boston, 2017), pp. 169–202.

[21] L. Greenman, P. J. Ho, S. Pabst, E. Kamarchik, D. A. Mazziotti, and R. Santra, Implementation of the time-dependent configuration-interaction singles method for atomic strong-field processes, Phys. Rev. A **82**, 023406 (2010).

[22] N. Rohringer, A. Gordon, and R. Santra, Configuration-interaction-based time-dependent orbital approach for *ab initio* treatment of electronic dynamics in a strong optical laser field, Phys. Rev. A **74**, 043420 (2006).

[23] B. Sheehy and L. F. DiMauro, Atomic and molecular dynamics in intense optical fields, Annu. Rev. Phys. Chem. **47**, 463 (1996).

[24] M. Protopapas, C. H. Keitel, and P. L. Knight, Atomic physics with super-high intensity lasers, Rep. Prog. Phys. **60**, 389 (1997).

[25] S. Pabst and R. Santra, XCID: A program package for multichannel ionization dynamics, Rev. 314, with contributions from P. J. Ho, CFEL, DESY, Hamburg, Germany, 2011.

[26] S. Pabst, D. Wang, and R. Santra, Driving Rabi oscillations at the giant dipole resonance in xenon, Phys. Rev. A **92**, 053424 (2015).

[27] L. Greenman, C. P. Koch, and K. B. Whaley, Laser pulses for coherent xuv raman excitation, Phys. Rev. A **92**, 013407 (2015).

[28] M. Sabbar, H. Timmers, Y.-J. Chen, A. K. Pymer, Z.-H. Loh, S. G. Sayres, S. Pabst, R. Santra, and S. R. Leone, State-resolved attosecond reversible and irreversible dynamics in strong optical fields, Nat. Phys. **13**, 472 (2017).

[29] A. Karamatskou and R. Santra, Time-dependent configuration-interaction-singles calculation of the $5p$-subshell two-photon ionization cross section in xenon, Phys. Rev. A **95**, 013415 (2017).

[30] S. Pabst, A. Sytcheva, A. Moulet, A. Wirth, E. Goulielmakis, and R. Santra, Theory of attosecond transient-absorption spectroscopy of krypton for overlapping pump and probe pulses, Phys. Rev. A **86**, 063411 (2012).

[31] S. Pabst, L. Greenman, D. A. Mazziotti, and R. Santra, Impact of multichannel and multipole effects on the Cooper minimum in the high-order-harmonic spectrum of argon, Phys. Rev. A **85**, 023411 (2012).

[32] A. Sytcheva, S. Pabst, S.-K. Son, and R. Santra, Enhanced nonlinear response of Ne^{8+} to intense ultrafast x rays, Phys. Rev. A **85**, 023414 (2012).

[33] A. Szabo and N. S. Ostlund, *Modern Quantum Chemistry: Introduction to Advanced Electronic Structure Theory*, 1st ed. (Dover, Mineola, 1996).

[34] S. Pabst, A. Sytcheva, O. Geffert, and R. Santra, Stability of the time-dependent configuration-interaction-singles method in the attosecond and strong-field regimes: A study of basis sets and absorption methods, Phys. Rev. A **94**, 033421 (2016).

[35] D. Krebs, S. Pabst, and R. Santra, Introducing many-body physics using atomic spectroscopy, Am. J. Phys. **82**, 113 (2014).

[36] T. Sato, T. Teramura, and K. Ishikawa, Gauge-invariant formulation of time-dependent configuration interaction singles method, Appl. Sci. **8**, 433 (2018).

[37] T. Teramura, T. Sato, and K. L. Ishikawa, Implementation of a gauge-invariant time-dependent configuration-interaction-singles method for three-dimensional atoms, Phys. Rev. A **100**, 043402 (2019).

[38] J. Butcher, *Numerical Methods for Ordinary Differential Equations*, 3rd ed. (Wiley, Chichester, 2016).

[39] E. Saldin, E. Schneidmiller, and M. Yurkov, *The Physics of Free Electron Lasers* (Springer, Berlin, Heidelberg, 2000).

[40] M. M. Abdullah, Anurag, Z. Jurek, S.-K. Son, and R. Santra, Molecular-dynamics approach for studying the nonequilibrium behavior of x-ray-heated solid-density matter, Phys. Rev. E **96**, 023205 (2017).

[41] R. Jin, M. M. Abdullah, Z. Jurek, R. Santra, and S.-K. Son, Transient ionization potential depression in nonthermal dense plasmas at high x-ray intensity, Phys. Rev. E **103**, 023203 (2021).

[42] K. Persson, The Materials Project, Materials Data on Ge (SG:227) by Materials Project, United States: N. p. (2020), doi:10.17188/1206032.

[43] S.-K. Son, R. Thiele, Z. Jurek, B. Ziaja, and R. Santra, Quantum-Mechanical Calculation of Ionization-Potential Lowering in Dense Plasmas, Phys. Rev. X **4**, 031004 (2014).

[44] M. Dondera and H. Bachau, Exploring above-threshold ionization of hydrogen in an intense x-ray laser field through nonperturbative calculations, Phys. Rev. A **85**, 013423 (2012).

[45] V. Florescu, O. Budriga, and H. Bachau, Two-photon above-threshold ionization of hydrogen over the photon energy range from 15 eV to 50 keV, Phys. Rev. A **84**, 033425 (2011).

[46] N. Rohringer and R. Santra, Multichannel coherence in strong-field ionization, Phys. Rev. A **79**, 053402 (2009).

[47] W. Zernik, Two-photon ionization of atomic hydrogen, Phys. Rev. **135**, A51 (1964).

[48] L. B. Madsen and P. Lambropoulos, Scaling of hydrogenic atoms and ions interacting with laser fields: Positronium in a laser field, Phys. Rev. A **59**, 4574 (1999).

[49] S. Klarsfeld, Two-photon ionization of atomic hydrogen in the ground state, Lett. Nuovo Cimento Soc. Ital. Fis. **3**, 395 (1970).

[50] J. Hofbrucker, A. V. Volotka, and S. Fritzsche, Relativistic calculations of the nonresonant two-photon ionization of neutral atoms, Phys. Rev. A **94**, 063412 (2016).

[51] P. Koval, S. Fritzsche, and A. Surzhykov, Relativistic and retardation effects in the two-photon ionization of hydrogen-like ions, J. Phys. B **36**, 873 (2003).

[52] E. P. Kanter, B. Krässig, Y. Li, A. M. March, P. Ho, N. Rohringer, R. Santra, S. H. Southworth, L. F. DiMauro, G. Doumy, C. A. Roedig, N. Berrah, L. Fang, M. Hoener, P. H. Bucksbaum, S. Ghimire, D. A. Reis, J. D. Bozek, C. Bostedt, M. Messerschmidt *et al.*, Unveiling and Driving Hidden Resonances with High-Fluence, High-Intensity X-Ray Pulses, Phys. Rev. Lett. **107**, 233001 (2011).